PHYSICS OF FLUIDS **19**, 063601 (2007)

Characteristics of two-dimensional flow around a rotating circular cylinder near a plane wall

Ming Cheng[a)]
Institute of High Performance Computing, 1 Science Park Road, #01-01, The Capricorn, Singapore Science Park II, Singapore 117528

Li-Shi Luo[b)]
Department of Mathematics and Statistics and Center for Computational Sciences, Old Dominion University, Norfolk, Virginia 23529

(Received 13 October 2006; accepted 5 April 2007; published online 12 June 2007)

We simulate a two-dimensional incompressible flow around a rotating circular cylinder near a plane wall at the Reynolds number $\mathrm{Re}=200$ by using the lattice Boltzmann equation with multiple relaxation times. We investigate the flow pattern in the parameter space of the rotational rate $\gamma := \omega a/U$ and the normalized gap $h:=H/D$, where ω is the angular velocity of the cylinder, a and D are the cylinder radius and diameter, respectively, U is the inflow velocity, and H is the gap between the cylinder and the wall. We quantify the effects of γ and h on the hydrodynamic forces and the frequency of vortex shedding from the cylinder. Our results indicate that two critical values of h, h_{down} and h_{up}, exist, which depend on γ. The flow is steady when $h<h_{\mathrm{down}}$, while it has a wake of a regular vortex street when $h>h_{\mathrm{up}}$. When $h_{\mathrm{down}}<h<h_{\mathrm{up}}$, the flow is aperiodic. We observe that the mean drag coefficient $\bar{C}_D$ is a monotonically increasing function of h when $\gamma\leqslant 0$. When $\gamma>0$, $\bar{C}_D$ is no longer a monotonic function of h. The mean drag coefficient $\bar{C}_D$ varies significantly in the range $h_{\mathrm{down}}<h<h_{\mathrm{up}}$, and so do the root-mean-square values of the lift and drag coefficients, $\tilde{C}_D$ and $\tilde{C}_L$. When $h>h_{\mathrm{up}}$, the wall effect diminishes. © *2007 American Institute of Physics*.
[DOI: 10.1063/1.2738608]

I. INTRODUCTION

The flow around a rotating circular cylinder is a problem of both theoretical and applied interest. When a cylinder rotates in a uniform flow, on the one side of the cylinder the tangential velocity is parallel to the free-streaming velocity whereas on the other side it is unparallel to the free-streaming velocity. This creates an asymmetry in the velocity and pressure fields around the rotating cylinder, which results in a force on the cylinder normal to the flow direction. This phenomenon is the well-known Magnus effect,[1] which is relevant to applications such as ship propulsion and boundary control on airfoil.

There have been numerous detailed studies of flow past an isolated rotating circular cylinder in two dimensions (2D).[2–7] For this flow, an important parameter is the rotation rate $\gamma:=a\omega/U$, which is the tangential speed $a\omega$ normalized by the free-stream velocity U, where a and ω are the cylinder radius and angular velocity, respectively. It has been shown that when $\gamma>0$ is below a critical value, depending on the Reynolds number Re, a Kármán vortex street is shed behind the cylinder.[2–7] The mean lift and drag coefficients and the Strouhal number increase about linearly with the rotation rate γ. When the rotation rate γ is greater than the critical value, the Kármán vortex shedding is extinct and the flow becomes steady. As γ increases further, there is a narrow range of γ in which the vortex shedding recurs. Beyond this narrow range of γ, the rotation of the cylinder completely dominates the flow: the flow becomes steady, the flow structure around the cylinder become self-similar, and the lift and drag coefficients eventually approach their asymptotic values predicted by potential flow theory.[7–9] The flow characteristics are dictated by the interaction of the boundary layer generated at the cylinder surface and the mean flow.[7] These would be significantly altered when the rotating cylinder is positioned closed to a flat plate. The presence of a plane wall in the flow breaks the flow symmetry and also leads to complicated interactions among the boundary layers separating from the cylinder and the plate. These interactions in turn will affect the flow patterns in the wake behind the cylinder.

Flow past a cylinder near a wall presents an interesting case for studying the boundary layers interactions and their effects and has been a subject of extensive investigation.[10–18] It has been experimentally observed that the vortex shedding of a stationary cylinder near to a plane wall can be dramatically altered by varying the gap between the cylinder and the plane wall.[10–18] The earliest experiments of the flow past a stationary circular cylinder close to a wall at a low Reynolds number $\mathrm{Re}=170$ were conducted by Taneda.[16] He found that when the normalized gap $h:=H/D=0.1$, only a single row of vortices was shed from the cylinder; when $h=0.6$, a regular double-row of vortices was shed. Similar work was carried out later by Bearman and Zdravkovich[10,18] for moderately high Reynolds numbers ($3.55\times 10^3\leqslant\mathrm{Re}\leqslant 4.5\times 10^4$). They found that when $h>0.3$, regular vortex shedding occurred,

---

[a)] Electronic mail: chengm@ihpc.a-star.edu.sg

[b)] Telephone: +1 (757) 683-5295. Fax: + 1 (757) 683-3885. Electronic mail: lluo@odu.edu and the Strouhal number, St, was almost independent of h. In addition, regular vortex shedding was suppressed when $h < 0.3$, although in some cases a weak vortex shedding signal was observed near the edge of the cylinder furthest away from the wall. When vortex shedding was suppressed, separation bubbles formed both upstream and downstream of the cylinder above the plate. When the cylinder touched the plate ($h=0$), upstream and downstream separation regions were attached to the cylinder and the downstream separation region contained two counter-rotating vortices separated by stagnant fluid. For higher Reynolds numbers ($8.6\times 10^4 \leqslant \mathrm{Re} \leqslant 3.0\times 10^5$), the effects due to cylinder surface roughness were investigated by Buresti and Lanciotti.[11] For a smooth cylinder, the critical value of h below which vortex shedding did not occur was between 0.3 and 0.4, however, for a roughened cylinder, the critical value was between 0.2 and 0.3. When the gap h is greater than the critical values, St was independent of h.

The effect of boundary layer thickness of the plane wall on the vortex shedding was considered by Grass *et al.*,[13] Taniguchi and Miyakoshi,[17] and Lei *et al.*[14] Recently, Cheng *et al.*[12] conducted flow visualization and vortex shedding frequency measurements at $\mathrm{Re}=500$ and $0 \leqslant h \leqslant 5.0$. They observed that for $h < 1.25$, only a street of single vortices shed from the cylinder, and St increased with h to a maximum value of 0.252 at $h \approx 1.25$. Both symmetric and asymmetric vortex shedding occurred for $h > 1.25$. When $h > 2.0$, St reached a constant about 0.2. More recently, using particle image velocimetry and hot-film anemometry, Price *et al.*[15] studied the flow around a stationary circular cylinder near a plane wall for Reynolds numbers between 1200 and 4960, $0 \leqslant h \leqslant 2.0$. Their results showed that for very small gaps ($h \leqslant 0.125$) the gap flow is extremely weak if not completely suppressed, and separation of the boundary layer occurs both upstream and downstream of the cylinder. With small gaps ($0.125 < h < 0.5$), the flow is similar to that with very small gaps ($h < 0.125$), except that there is now a pronounced pairing between the wall shear-layer and that shed from the inner side of the cylinder. At intermediate gaps ($0.5 < h < 0.75$), the flow are characterized by the onset of vortex shedding from the cylinder. When $h > 1$, there is no separation of the wall boundary layer, either upstream or downstream of the cylinder. Following the work of Price *et al.*,[15] Dipankar and Sengupta[19] carried out numerical simulations for the flow past a circular cylinder in the vicinity of a plane wall at $\mathrm{Re}=1200$, and their numerical results agreed well with the experimental results.[15]

Vortex shedding and wake development behind a rotating circular cylinder near a plane wall are much more complicated than that of a stationary cylinder, and the fluid dynamic characteristics would differ from those of either an isolated rotating circular cylinder or a stationary circular cylinder near a plane wall. A literature survey reveals, however, that there are few published accounts about the effects of a plane wall on the vortex shedding mechanism and wake patterns behind a rotating cylinder. The study of vortex shedding and wake development behind a rotating circular cylinder adjacent to a plane wall would undoubtedly deepen our understanding about some important phenomena in flow-structure interactions, such as the cause of vortex-induced vibration and its suppression and control.[20]

The flow around a rotating circular cylinder near a plane wall depends mainly on four parameters: the Reynolds number Re, the boundary layer thickness on the plane wall, the rotation rate γ of the cylinder, and the gap between the cylinder and the plane wall H. In this work, we confine our study to the influence of the boundary layer thickness on the flow and will only investigate the effects on the flow due to both the normalized gap $h := H/D$ and the rotational rate $\gamma := \omega a/U$, where H, D, a, ω and U are the gap between the cylinder and the flat plane, the cylinder diameter, the cylinder radius, the angular velocity of the rotating cylinder, and the inflow velocity, respectively. The Reynolds number is fixed at $\mathrm{Re}=200$. At this Reynolds number, we can assume that the flow is two-dimensional and laminar. It is well known that for flow past a stationary circular cylinder, the onset of three-dimensional wake structures occurs at $\mathrm{Re} \approx 180$.[21] However, for a rotational circular cylinder, it is believed that the critical Reynolds number for the onset of three-dimensional flow structures is higher than 180, because of the rotation of the cylinder. This is supported by both numerical and experimental observations.[2–4] By interrogating the numerical results, we reveal the dependence on h and γ of the vortex shedding development associated with the Kármán vortex street behind the cylinder, the pressure distributions around the cylinder, the lift and drag forces exerting on the cylinder. We will use the lattice Boltzmann equation (LBE) with multiple-relaxation-time (MRT) collision model[22–25] to perform the numerical simulations.

The remainder of this paper is organized as follows: Sec. II provides a succinct introduction of the MRT-LBE, the boundary and initial conditions, and validation by using the flow of an impulsively started rotating circular cylinder. Section III presents our numerical results, which include streak lines, vorticity contours, velocity field, the surface pressure distribution, time histories of the drag and lift coefficients and their ratio, and the averaged and root-mean-square of the drag and lift coefficients as functions of h and γ. And finally, Sec. IV concludes the paper.

II. NUMERICAL METHOD

The lattice Boltzmann equation (LBE) is an alternative to conventional computational fluid dynamics (CFD) methods based on the Navier-Stokes equations. It is based on the Boltzmann equation (or kinetic theory) for the single particle velocity distribution function.[26,27] Unlike traditional numerical methods, which solve for the macroscopic variables such as density, velocity, and temperature, the LBE obtains these variables from the moment integrations of the distribution function. As such, the LBE has some computational advantages because it is based on the Boltzmann equation with a linear advection term, as opposed to the Navier-Stokes equation with a nonlinear advection term.[28]

A. Lattice Boltzmann equation

In what follows, we shall use the generalized lattice Boltzmann equation (GLBE), or lattice Boltzmann equation

(LBE) with the multiple-relaxation-time (MRT) collision model.[23] The evolution equation for the MRT-LBE of Q velocities on a D-dimensional lattice $\boldsymbol{x}_i \in \delta_x \mathbb{Z}^D$ with discrete time $t_n \in \delta_t \mathbb{N}_0 := \delta_t\{0,1,\ldots\}$ is

$$\mathbf{f}(\boldsymbol{x}_i + \boldsymbol{c}\,\delta_t, t_n + \delta_t) - \mathbf{f}(\boldsymbol{x}_i, t_n) = \boldsymbol{\Omega}(\boldsymbol{x}_i, t_n)$$

$$= -\mathsf{M}^{-1} \cdot \hat{\mathsf{S}} \cdot [\mathbf{m} - \mathbf{m}^{(\mathrm{eq})}], \tag{1}$$

where M is a $Q \times Q$ matrix which linearly transforms the distribution functions $\mathbf{f} \in \mathbb{V} \equiv \mathbb{R}^Q$ to the velocity moments $\mathbf{m} \in \mathbb{M} \equiv \mathbb{R}^Q$:

$$\mathbf{m} = \mathsf{M} \cdot \mathbf{f}, \quad \mathbf{f} = \mathsf{M}^{-1} \cdot \mathbf{m}, \tag{2}$$

and $\hat{\mathsf{S}}$ a non-negative $Q \times Q$ diagonal relaxation matrix.[24] The boldface symbols denote column vectors as the following:

$$\mathbf{f}(\boldsymbol{x}_i + \boldsymbol{c}\,\delta_t, t_n + \delta_t) = (f_0(\boldsymbol{x}_i, t_n + \delta_t), \ldots, f_b(\boldsymbol{x}_i + \boldsymbol{c}_b \delta_t, t_n + \delta_t))^{\mathsf{T}},$$

$$\mathbf{f}(\boldsymbol{x}_i, t_n) = (f_0(\boldsymbol{x}_i, t_n), f_1(\boldsymbol{x}_i, t_n), \ldots, f_b(\boldsymbol{x}_i, t_n))^{\mathsf{T}},$$

$$\mathbf{m} = (m_0(\boldsymbol{x}_i, t_n), m_1(\boldsymbol{x}_i, t_n), \ldots, m_b(\boldsymbol{x}_i, t_n))^{\mathsf{T}},$$

$$\mathbf{m}^{(\mathrm{eq})} = (m_0^{(\mathrm{eq})}(\boldsymbol{x}_i, t_n), m_1^{(\mathrm{eq})}(\boldsymbol{x}_i, t_n), \ldots, m_b^{(\mathrm{eq})}(\boldsymbol{x}_i, t_n))^{\mathsf{T}},$$

where T is the transpose operator and $b := (Q-1)$.

For the sake of simplicity, we will restrict ourselves to the nine-velocity model in two dimensions (D2Q9 model). The discrete velocities $\{\boldsymbol{c}_i\}$ are

$$\boldsymbol{c}_i = \begin{cases} (0,\ 0), & i = 0, \\ (\pm 1,\ 0)c,\ (0,\ \pm 1)c, & i = 1,\ 2,\ 3,\ 4, \\ (\pm 1,\ \pm 1)c, & i = 5,\ 6,\ 7,\ 8, \end{cases} \tag{3}$$

where $c = \delta_x / \delta_t$. A particular order of moments used here is[24]

$$\mathbf{m} = (\rho, e, \varepsilon, j_x, q_x, j_y, q_y, p_{xx}, p_{xy})^{\mathsf{T}}, \tag{4}$$

in which ρ is the mass density, and $j_x = \rho u_x$ and $j_y = \rho u_y$ are x and y components of the flow momentum $\boldsymbol{j}$, respectively, which are the conserved moments in the system. Other moments are nonconserved moments and their equilibria are functions of the conserved moments in the system.[22–25] With the above order of moments, the corresponding diagonal relaxation matrix of relaxation rates $\{s_i\}$ is

$$\hat{\mathsf{S}} = \mathrm{diag}(s_\rho, s_e, s_\varepsilon, s_\chi, s_q, s_\chi, s_q, s_\nu, s_\nu). \tag{5}$$

In the usual LBE simulations, because ρ, j_x and j_y are conserved quantities, the relaxation rates s_ρ and s_χ have no effect on the system and therefore can assume any value. However, if an external force is present, its effect is influenced by the value of s_χ. The relaxation rates s_ν and s_e determine the shear and bulk viscosities, respectively. In the presence of solid boundaries, s_q affects the exact locations where the no-slip boundary conditions are satisfied.[29–32]

For the D2Q9 model with the particular moment ordering given by Eq. (4), the transformation matrix M is given by[24]

$$\mathsf{M} = \begin{pmatrix} 1 & 1 & 1 & 1 & 1 & 1 & 1 & 1 & 1 \\ -4 & -1 & -1 & -1 & -1 & 2 & 2 & 2 & 2 \\ 4 & -2 & -2 & -2 & -2 & 1 & 1 & 1 & 1 \\ 0 & 1 & 0 & -1 & 0 & 1 & -1 & -1 & 1 \\ 0 & -2 & 0 & 2 & 0 & 1 & -1 & -1 & 1 \\ 0 & 0 & 1 & 0 & -1 & 1 & 1 & -1 & -1 \\ 0 & 0 & -2 & 0 & 2 & 1 & 1 & -1 & -1 \\ 0 & 1 & -1 & 1 & -1 & 0 & 0 & 0 & 0 \\ 0 & 0 & 0 & 0 & 0 & 1 & -1 & 1 & -1 \end{pmatrix},$$

which can be constructed from the monomials of velocity components $c_{i,\alpha}^n c_{j,\beta}^m \cdots c_{k,\gamma}^l$, where α, β, and $\gamma \in \{x, y\}$, by using the Gramd-Schmit orthogonalization procedure.[22–24]

To reduce the effect of round-off error, we use the density fluctuation $\delta\rho$ and assume the mean density $\bar{\rho} = 1$. The total density is therefore $\rho = \bar{\rho} + \delta\rho$. In addition, we use $\boldsymbol{j} = \bar{\rho}\boldsymbol{u}$ to reduce effects due to compressibility.[33] Thus the conserved quantities in an *athermal* LBE model and the corresponding equilibria are

$$\delta\rho^{(\mathrm{eq})} = \delta\rho = \sum_i f_i, \quad \boldsymbol{j}^{(\mathrm{eq})} = \boldsymbol{j} := (j_x, j_y) = \bar{\rho}\boldsymbol{u} = \sum_i f_i \boldsymbol{c}_i. \tag{6}$$

For the *athermal* D2Q9 model in which the internal energy is *not* a conserved quantity, the equilibria for nonconserved moments are[24]

$$e^{(\mathrm{eq})} = -2\alpha_2 \delta\rho + 3(j_x^2 + j_y^2), \quad \varepsilon^{(\mathrm{eq})} = \delta\rho - 3(j_x^2 + j_y^2), \tag{7a}$$

$$\boldsymbol{q}^{(\mathrm{eq})} = (q_x^{(\mathrm{eq})}, q_y^{(\mathrm{eq})}) = -\boldsymbol{j} = -(j_x, j_y), \tag{7b}$$

$$p_{xx}^{(\mathrm{eq})} = j_x^2 - j_y^2, \quad p_{xy}^{(\mathrm{eq})} = j_x j_y. \tag{7c}$$

With the above equilibria, the LBE system of Eq. (1) leads to the *incompressible* Navier-Stokes equations in the limit of small Mach number and large system size. If we choose $\alpha_2 = 1$ and set all the relaxation rates $\{s_i\}$ to a single value of $1/\tau$, i.e., $s_i = 1/\tau \forall i$, then the MRT-LBE reduces to the corresponding lattice Bhatnagar-Gross-Krook[34] (LBGK) equation.[35,36]

For the D2Q9 MRT-LBE model, the speed of sound c_s, the shear viscosity ν and the bulk viscosity ζ are given by[24]

$$c_s^2 = \frac{1}{3}(2 - \alpha_2), \quad \nu = \frac{1}{3}\left(\frac{1}{s_\nu} - \frac{1}{2}\right), \quad \zeta = \frac{\alpha_2}{6}\left(\frac{1}{s_e} - \frac{1}{2}\right). \tag{8}$$

It is apparent that when $\alpha_2 = 1$ and $s_\nu = s_e = 1/\tau$, we have $\zeta = \nu/2$ for the lattice BGK (LBGK) model. We would like to point out that this is one primary reason responsible for the numerical instability of the LBGK model, because for high Reynolds number flows ν is very small, and the bulk viscosity ζ is even smaller and thus insufficient to dissipate spurious density fluctuations in the system.

B. Boundary and initial conditions

Figure 1 shows the computational domain for a two-dimensional flow of a viscous incompressible fluid of constant velocity U past a rotating circular cylinder of radius a near a plane wall. The computational domain is a rectangle

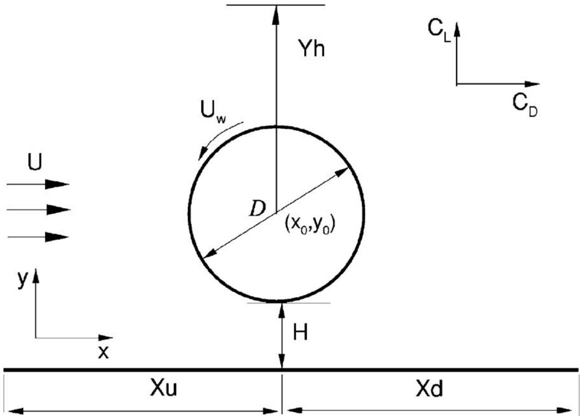

FIG. 1. Flow configuration schematics.

of size $(X_d+X_u)\times(H+a+Y_h)$, as depicted in Fig. 1. The boundary conditions are given: an inflow boundary at the left, a free outflow boundary at the right, a free-slip boundary at the top and a wall boundary at the bottom. The inflow boundary condition is given by

$$f_i = f_i^{(\mathrm{eq})}(\rho=\bar{\rho}, \boldsymbol{u}=(U,0)). \tag{9}$$

At the outflow boundary, owing to the sufficiently large domain behind the cylinder, no influence is expected for the results, a fixed pressure is imposed through the equilibria at the outlet, and the velocity is extrapolated downstream.

The no-slip conditions in the LBE are realized with the bounce-back boundary conditions in which all particles colliding with a solid wall not only reverse their momenta, but also gain the momentum imposed by the wall,[37]

$$f_{\bar{i}} = f_i - 6 w_i \rho \frac{\boldsymbol{c}_i \cdot \boldsymbol{U}_w}{c^2}, \tag{10}$$

where $f_{\bar{i}}$ is the distribution function of the velocity $\mathbf{c}_{\bar{i}} := -\boldsymbol{c}_i$, $\boldsymbol{U}_w$ is the wall velocity at the point where particle-wall collision takes place, and the coefficients $\{w_i\}$ for the D2Q9 model are $w_0=4/9$, $w_{1,2,3,4}=1/9$, and $w_{5,6,7,8}=1/36$.

Here, we use the potential flow past a circular cylinder as the initial velocity field,

$$\begin{aligned} u_0 &= \left\{ 1 - \frac{[(x_i-x_0)^2-(y_i-y_0)^2]a^2}{[(x_i-x_0)^2+(y_i-y_0)^2]^2} \right\} U, \\ v_0 &= -\frac{2(x_i-x_0)(y_i-y_0)a^2}{[(x_i-x_0)^2+(y_i-y_0)^2]^2} U, \end{aligned} \tag{11}$$

where x_0 and y_0 are the position of the cylinder center in the physical space, and

$$\mathbf{f} = \mathbf{f}^{(\mathrm{eq})}\big|^{t=0}_{\boldsymbol{u}_0=(u_0,v_0)} = \mathbf{M}\cdot\, \mathbf{m}^{(\mathrm{eq})}\big|^{t=0}_{\boldsymbol{u}_0=(u_0,v_0)}. \tag{12}$$

Because the LBE is only valid for near incompressible flow, we maintain the Mach number $\mathrm{Ma} := U/c_s < 0.15$ or $U < 0.15 c_s$ in the present work.[33] Since $c_s = 1/\sqrt{3}$ is a constant for the LBE model, $\mathrm{Ma} = U/c_s \approx 0.09$.

C. Validation: Flow past an impulsively started cylinder

The flow past an isolated rotating circular cylinder has been studied both numerically and experimentally.[2,3,7] We use this flow to validate the LBE model. The dimension of the computational domain are $L_x \times L_y = 60a \times 40a$, and the cylinder center is situated at the horizontal centerline of the domain and $20a$ downstream from the left. The cylinder radius $a = 40\delta_x$. Our previous experience indicated that this resolution is sufficient for the flow in the present work.[38] In this work, we use the "zig-zag" approximation to represent the curved boundary of the cylinder. Previous study[39] has shown that the "zig-zag" approximation is adequate for the resolution $a = 40\delta_x$ and the Reynolds number $\mathrm{Re}=200$ used in this work, and this will be shown quantitatively.

In our simulations, the relaxation rates s_e and s_ν are determined by the viscosity ν (or Re), $s_e = s_\nu = 1/\tau = (3\nu + 1/2) = (3DU/\mathrm{Re} + 1/2)$. Other relaxation rates are chosen as $s_\epsilon = 1.2$ and $s_q = 1.5$.[24] The Reynolds number (Re), lift (C_L) and drag (C_D) coefficients are defined as

$$\mathrm{Re} = \frac{UD}{\nu}, \quad C_L = \frac{F_L}{\frac{1}{2}\bar{\rho}U^2 D}, \quad C_D = \frac{F_D}{\frac{1}{2}\bar{\rho}U^2 D}, \tag{13}$$

where F_L and F_D are the lift and drag forces exerted by the fluid on a unit length of the cylinder, respectively. We compute C_L and C_D through the pressure coefficient C_p and the stress coefficient C_σ around the cylinder surface:

$$C_p = \frac{p - p_\infty}{\frac{1}{2}\bar{\rho}U^2}, \quad C_\sigma = \frac{\sigma}{\frac{1}{2}\bar{\rho}U^2}, \tag{14}$$

where

$$p - p_\infty = \frac{1}{3}(\rho - \bar{\rho}), \quad \sigma = \rho\nu \left(\partial_r u_\theta - \frac{u_\theta}{r} \right)_{r=a},$$

$$\partial_r u_\theta = \partial_x u_\theta \cos\theta + \partial_y u_\theta \sin\theta, \quad u_\theta := v\cos\theta - u\sin\theta,$$

$$(\partial_x u)_{i,j} = \frac{4u_{i+1,j} - u_{i+2,j} - 3u_{i,j}}{2\delta_x},$$

$$(\partial_y u)_{i,j} = \frac{4u_{i,j+1} - u_{i,j+2} - 3u_{i,j}}{2\delta_y}.$$

The drag and lift coefficients can be decomposed into the pressure and the shear-stress components as the following:

$$\begin{aligned} C_{Dp} &= -\frac{1}{2}\int_0^{2\pi} C_p(\theta)\cos\theta\, d\theta, \\ C_{D\sigma} &= -\frac{1}{2}\int_0^{2\pi} C_p(\theta)\sin\theta\, d\theta, \end{aligned} \tag{15a}$$

(a) $\gamma = 0.5$

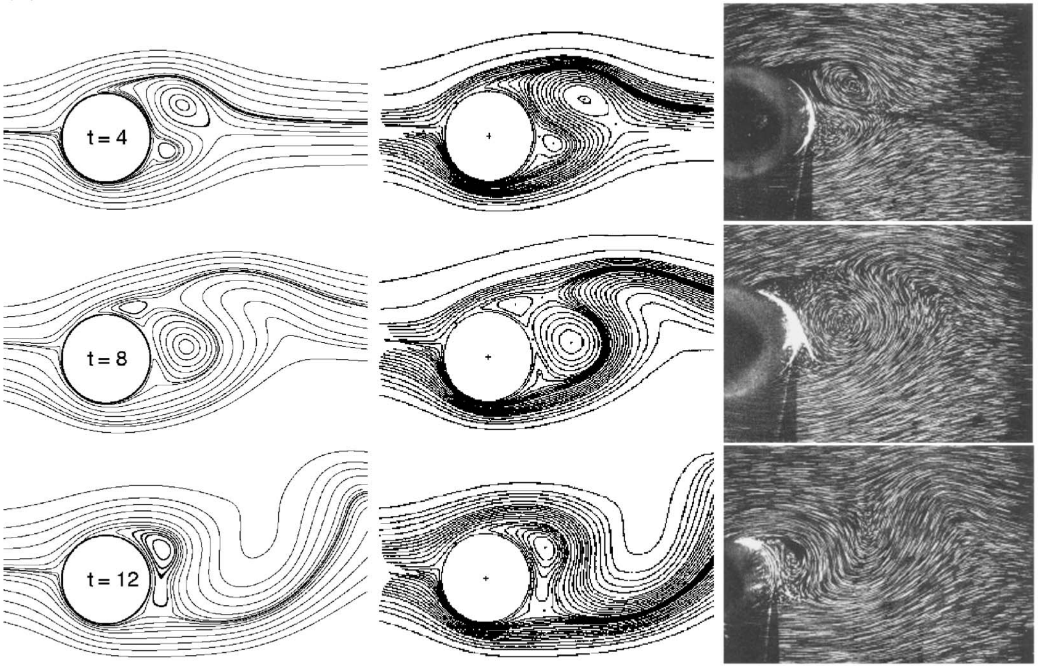

(b) $\gamma = 1.0$

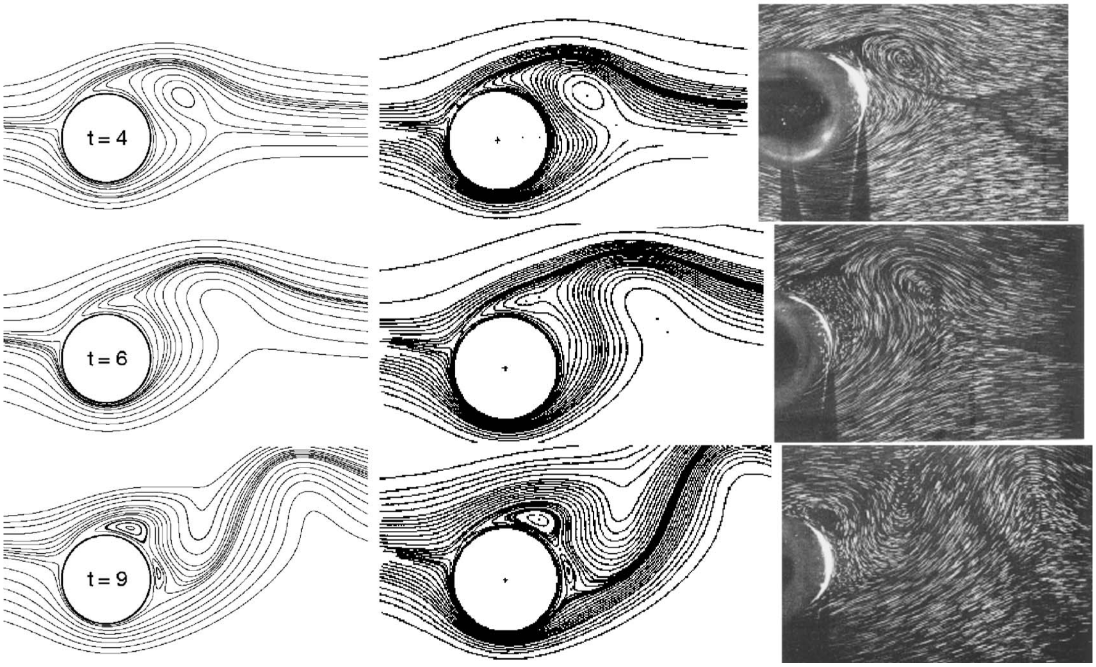

FIG. 2. Instantaneous streamlines of flow past an impulsively started rotating and moving circular cylinder at Re=200. (a) γ=0.5 and (b) γ=1.0. The results obtained by the LBM (left), semianalytical method (Ref. 2) (center), and experimental flow visualization (Ref. 2) (right) at different times.

$$C_{Lp} = -\frac{1}{2}\int_0^{2\pi} C_\sigma(\theta)\sin\theta d\theta,$$

$$C_{L\sigma} = \frac{1}{2}\int_0^{2\pi} C_\sigma(\theta)\cos\theta d\theta. \tag{15b}$$

The total drag and lift coefficients are then given by

$$C_D = C_{Dp} + C_{D\sigma}, \quad C_L = C_{Lp} + C_{L\sigma}. \tag{16}$$

Figure 2 shows the evolution of streamlines for the flow past an isolated rotating circular cylinder at Re=200, γ =0.5 and 1.0. We compare our LBE results with those obtained by a semianalytical method and experiments.[2,3] For the dimensionless time (in the units of U/a) in the interval $2 \leqslant t \leqslant 12$, Fig. 2 shows the agreement between the LBE results and the existing ones in terms of flow pattern.[2,3] The agreement is further quantified by comparing the time evolution of the velocity distribution along the centerline behind

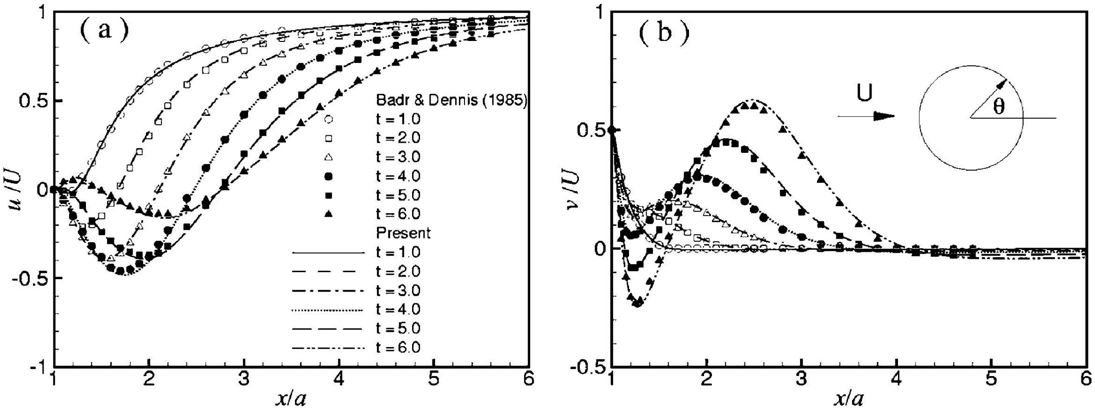

FIG. 3. Comparison of velocity profiles with the results of Badr and Dennis (Ref. 2) at Re=200 and $\gamma=0.5$. (a) The x component velocity on $\theta=0$. (b) The y component of velocity on $\theta=0$.

the cylinder in Fig. 3 and the drag and lift coefficients in Fig. 4 during the early stage of flow. Clearly, our results obtained by the LBE method agree very well with the existing ones obtained by the conventional methods.[2,3] Table I lists the mean drag ($\bar{C}_D$) and mean lift ($\bar{C}_L$) coefficients and the Strouhal number for the fully developed flow, obtained by the conventional CFD methods[3,7] and the LBE. The largest relative difference is about 2.2% in $\bar{C}_L$ at $\gamma=1.0$. For the rest, the relative differences are about or under 1%. This quantitatively validates the LBE method used in the present work.

III. RESULTS AND DISCUSSION

In this section we present our main results of simulations of the flow past a rotating circular cylinder near to a plane wall. The wall effect on the flow development behind a rotating circular cylinder at Re=200 is investigated by systematically varying the normalized gap h and the rotational rate γ, in the ranges of $-1 \leqslant \gamma \leqslant 1$ and $0 < h \leqslant 5.0$.

Our results are organized as the following: Sec. III A presents instantaneous streak lines of the flow, which allow us to categorize the flow pattern qualitatively. Section III B presents instantaneous vorticity contours of the flow, which allow us to quantitatively analyze the dynamics of the vortex shedding and wake evolution. Section III C shows the velocity field between the gap and the surface pressure distribution around the cylinder, which provide further information not so obvious in streak lines or vorticity contours. Finally, Sec. III D presents the results of the lift and drag coefficients, C_L and C_D. While flow fields, such as the vorticity contours and the velocity field, can show in great detail the flow information, it is the lift and drag forces which can be easily measured in experiments. It is therefore important to study how features of the flow field are reflected in C_L and C_D. We show the dependence on γ and h of C_L and C_D, including their time history, their time-averaged mean and root-mean-square (RMS) values and observe the features corresponding to changes in flow patterns.

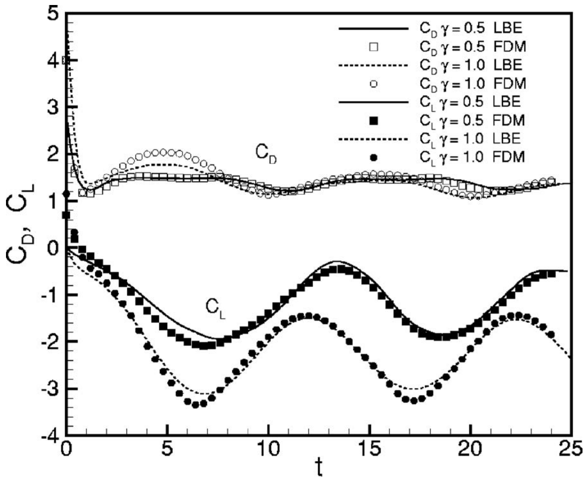

FIG. 4. Time evolution of the lift and drag coefficients for flow past an impulsively started rotating and translating circular cylinder at Re=200 and $\gamma=0.5$ and 1.0. The lines and symbols present the LBE and finite difference (Ref. 3) results, respectively.

A. Flow patterns

We first show in Figs. 5–8 the typical wake patterns represented by streak lines with varying gap height h and a fixed rotational rate γ. The flow pattern at $\gamma=0.5$ exhibits the following features. When $h=0.4$ [Fig. 5(a)], the streak lines at the back of the cylinder are substantially tilted upward and there is no vortex shedding in the wake. The wake is in steady state. The general flow pattern does not change much when the gap is narrower than $h<0.4$. However, the flow

TABLE I. Flow past a rotating cylinder at Re=200, $\gamma=0.5$ and 1.0. The mean drag and mean lift coefficients, $\bar{C}_D$ and $\bar{C}_L$, and the Strouhal number St, obtained by the finite difference (FD) method (Ref. 3), finite element (FE) method (Ref. 7), and the LBE method in the present work.

	$\gamma=0.5$			$\gamma=1.0$		
	$\bar{C}_D$	$\bar{C}_L$	St	$\bar{C}_D$	$\bar{C}_L$	St
FD[a]	1.28	−1.30	1.97	1.13	−2.30	1.94
FE[b]	1.27	−1.30	1.96	1.10	−2.20	1.93
LBE	1.28	−1.32	1.95	1.12	−2.25	1.93

[a] Reference 3.

[b] Reference 7.

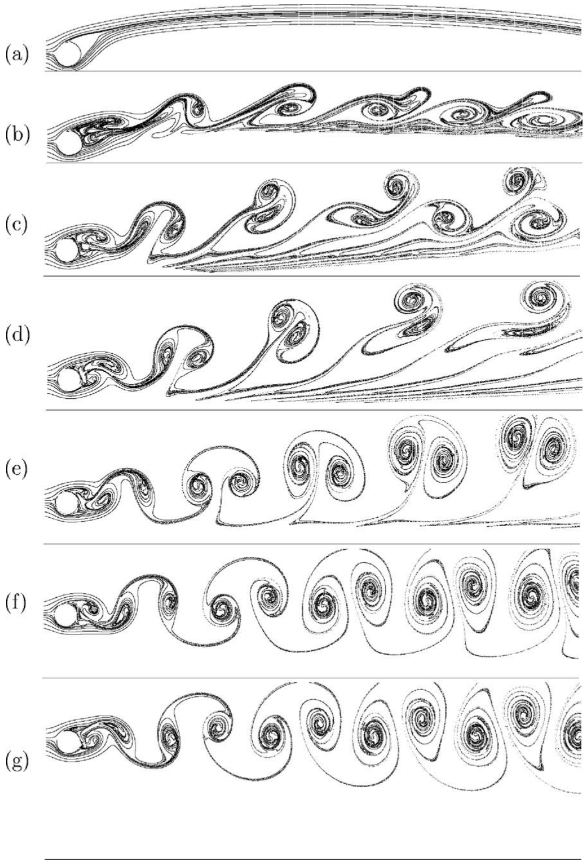

FIG. 5. Instantaneous streak lines of the flow past a rotating circular cylinder near a flat wall with Re=200, $\gamma=0.5$, and different h. (a) $h=0.4$, (b) $h=0.5$, (c) $h=0.8$, (d) $h=1.0$, (e) $h=1.5$, (f) $h=2.5$, and (g) $h=5.0$.

pattern changes significantly when the gap is larger than 0.4. First, the flow becomes unstable at $h=0.5$ [Fig. 5(b)]. The vortices are shed from the cylinder into the wake at an angle of roughly 30° with respect to the plane wall. An *aperiodic* vortex street appears in the wake slightly further away from the cylinder. When the gap increases to $h=0.8$ [Fig. 5(c)], the flow shows a striking feature of alternating vortices shed from the upper and lower sides of the cylinder. The sizes of vortices shed from the upper and lower sides of the cylinder are different, and the vortices shed from the lower side move faster downstream than those shed from the upper side. As h increases to 1.0, as shown in Fig. 5(d), the sizes of vortices shed alternatively from the upper and lower sides of the cylinder remain different, the former is more round in shape while the latter is more oblate, but the vortex structure behind the cylinder tends to be a more regular arrangement. One interesting feature to note is that the center line of the vortex street and the plane wall form a notable angle. This angle is reduced as h increases further. When h increases to 1.5 and beyond, the flow behind the cylinder is characterized by a Kármán vortex street consisting of regular alternating vortices, as shown in Figs. 5(e) and 5(f). The distance between consecutive vortices remains almost constant. Obviously the wall effect on the vortex shedding decreases with increasing h. When $h>2.5$, the flow pattern resembles that of wall-free vortex shedding, as shown in Fig. 5(g).

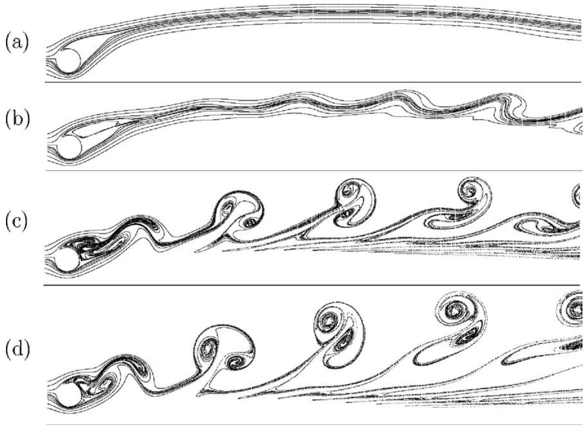

FIG. 6. Similar to Fig. 5 with $\gamma=1.0$. (a) $h=0.6$, (b) $h=0.7$, (c) $h=0.8$, and (d) $h=1.0$.

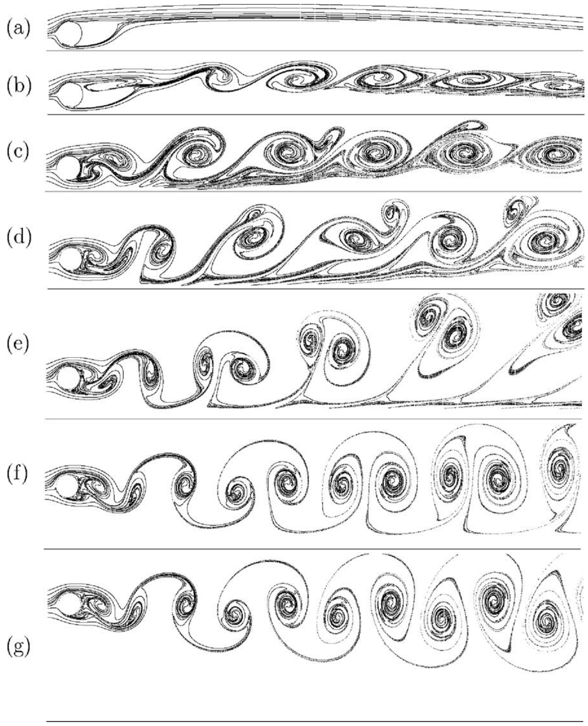

FIG. 7. Similar to Fig. 5, with $\gamma=-0.5$. (a) $h=0.4$, (b) $h=0.5$, (c) $h=0.7$, (d) $h=1.0$, (e) $h=1.5$, (f) $h=2.5$, and (g) $h=5.0$.

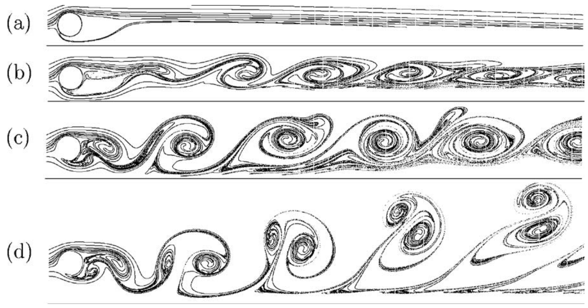

FIG. 8. Similar to Fig. 5 with $\gamma=1.0$. (a) $h=0.6$, (b) $h=0.7$, (c) $h=1.0$, and (d) $h=1.5$.

Figure 6 shows the evolution of flow pattern at $\gamma=1.0$ with varying h, similar to Fig. 5. The higher rotational rate does not change the general feature of the flow evolution, that is, the flow evolves from a steady to unsteady flow, then to a regular periodic vortex shedding flow. However, γ does affect the values of h at which the transitions between different flow regimes take place. For instance, at $\gamma=1.0$, the steady-unsteady flow transition occurs at $h\approx 0.7$, as shown in Fig. 6(b), as opposed to $h\approx 0.4$ for $\gamma=0.5$. In addition, the recirculation zone behind the cylinder on the plane wall is larger than that of $\gamma=0.5$. We also note that the flow patterns at $h=1.0$ with $\gamma=0.5$ and 1.0 are rather similar, as shown in Fig. 5(d) and Fig. 6(d), respectively. However, the vortices shed from the upper side of the cylinder are stronger when $\gamma=1.0$. As the gap h widens, the influence due to increased γ (from 0.5 to 1.0) diminishes.

Figures 7 and 8 present the flow patterns with clockwise rotating cylinder ($\gamma<0$) for $\gamma=0.5$ and 1.0, respectively. The main effect duo to the reverse of the cylinder rotation from counterclockwise ($\gamma>0$) to clockwise ($\gamma<0$) is the suppression of the flow through the gap between the cylinder and the flat plat. The viscous effect reduces the flow velocity through the gap, while accelerating the flow on the top of the cylinder. The smaller the gap, the more severe the viscous effect.

As h decreasing and with $\gamma<0$ fixed, the flow encounters a increasing resistance to pass through the gap. Consequently, when h is small enough, the flow behaves like the flow past a surface-mounted stationary obstacle with an effective size larger than the rotating cylinder, as shown in Fig. 7(a). This phenomenon has also been observed experimentally by Bearman and Zdravkovich[10] in the flow past a stationary cylinder near a plate, but the recirculation zone behind a rotating cylinder with $\gamma<0$ near a plate is much smaller than that behind a stationary cylinder near a plate. When $h=0.5$, a single row of same-sign vortices is shed, as shown in Fig. 7(b). When $0.5<h<1.5$, the vortex structure changes from the single row of same-sign vortices to a string of alternate signed vortices as h increases. It is worth noting that the flow patterns behind the cylinder at $h=0.7$ and 1.0, as shown in Figs. 7(c) and 7(d), respectively, are similar to those at $h=0.5$ and 0.8 for $\gamma=0.5$, as shown in Figs. 5(b) and 5(c), respectively, except that the length of vortex formation is shorter and the vortex trajectory in the wake is closer to the wall. This indicates that the flow stability is affected by the direction of rotation. When h increases to 1.5, regular double-row vortices are shed into wake, as shown in Fig. 7(e). As h further increases, the regular alternate vortex shedding and the Kármán vortex street appear behind the cylinder, as shown Figs. 7(f) and 7(g).

Similar to Fig. 7, Fig. 8 shows the flow pattern for $\gamma=-1.0$. Once again, the evolution of the flow pattern with varying h is influenced by the magnitude of γ. Comparing similar vortex structures shown in Fig. 8 with Fig. 7, we observe that flow pattern with a larger h at $\gamma=-1.0$ corresponds to a similar flow pattern with smaller h at $\gamma=-0.5$. This is because the presence of the rotation and the plane wall has the effect of reducing the roll-up vortex on the lower side of the cylinder. Thus, increasing the rotational rate or decreasing the gap can enhance this effect.

Our results indicate the existence of two critical values in the gap h, h_{down} and h_{up}, which depend on γ ($h_{\mathrm{down}}\approx 0.4$ and $h_{\mathrm{up}}\approx 1.5$ for $\gamma=0.5$, and $h_{\mathrm{down}}\approx 0.6$ and $h_{\mathrm{up}}\approx 1.5$ for $\gamma=1.0$). They divide the flow into three different regimes: steady, irregular vortex shedding, and regular vortex shedding. When $h<h_{\mathrm{down}}$, the flow is steady. When $h>h_{\mathrm{up}}$, the wake becomes a regular vortex street. When $h_{\mathrm{down}}<h<h_{\mathrm{up}}$, the flow appears to be an irregular complex vortex structure. We also observe that while h_{down} strongly depends on both the sign and magnitude of γ, h_{up} shows a very week dependence on γ.

B. Vortex shedding and wake evolution

Vortex shedding is a key characteristic of interest here. We will next investigate the dependence on γ and h of the vortex-shedding evolution process in the near-wake region by studying the vorticity field. Figures 9 and 10 show some typical evolution patterns of the vorticity field, in which positive and negative vorticities are represented by solid and dashed lines, respectively.

Figure 9 shows the process of vortices shedding from the cylinder for $\gamma=0.5$, $h=0.5$ (left) and 1.0 (right) in one shedding cycle of period T. The initial time $T_0=0$ is arbitrary. When $t=0$, as shown in Fig. 9(a)(left), a vortex pair is generated in the near wake and is ready to move downstream. A negative vortex has rolled up on the upper side of the cylinder. A group of three vortices consisting of one positive vortex from the lower side of the cylinder and two negative vortices from the upper side of the cylinder and the plane wall is just being shed from the cylinder. The vorticity generated from the lower side of the cylinder and the flow accelerated between the gap are responsible for the vorticity growth in the boundary layer on the plane wall. Because of the coupling between the wake and the boundary layer, the vortex separating from the lower side of the cylinder is stretched by vorticity of opposite sign close to the plane wall as time goes to $t=T/5$, as shown in Fig. 9(b)(left). A second negative vortex is generated, with the vortex induced on the plane wall as well, while the first negative vortex still remains attached to the cylinder. In the meantime, a pair of vortices with opposite signs form a thin sheet, which is pushed by the gap jet to move away from the cylinder at an angle tilting away from the wall. At $t=2T/5$, a vortex pair of two opposite-signed vortices is created, as shown in Fig. 9(c)(left), and the vortex pair is swept downstream at $t=3T/5$, as shown in Fig. 9(d)(left). The shapes of shedding vortices are grouped as a round vortex pair followed by a slender negative vortex. The vortex-pair evolves into a single negative vortex as it moving downstream: The positive vortex dissipates faster than its negative partner, and eventually disappears so that only the negative vortex survives to form a single row of same-sign vortices in the wake slightly further away from the cylinder, as shown in Fig. 5(b).

Figure 9, right column, shows the vorticity contours with $\gamma=0.5$ and $h=1.0$. First, at $t=0$, a negative vortex just appears on the top of the cylinder and a positive one is rolling up at the bottom of the cylinder. Slightly downstream, a positive-negative vortex pair shed from the cylinder and a

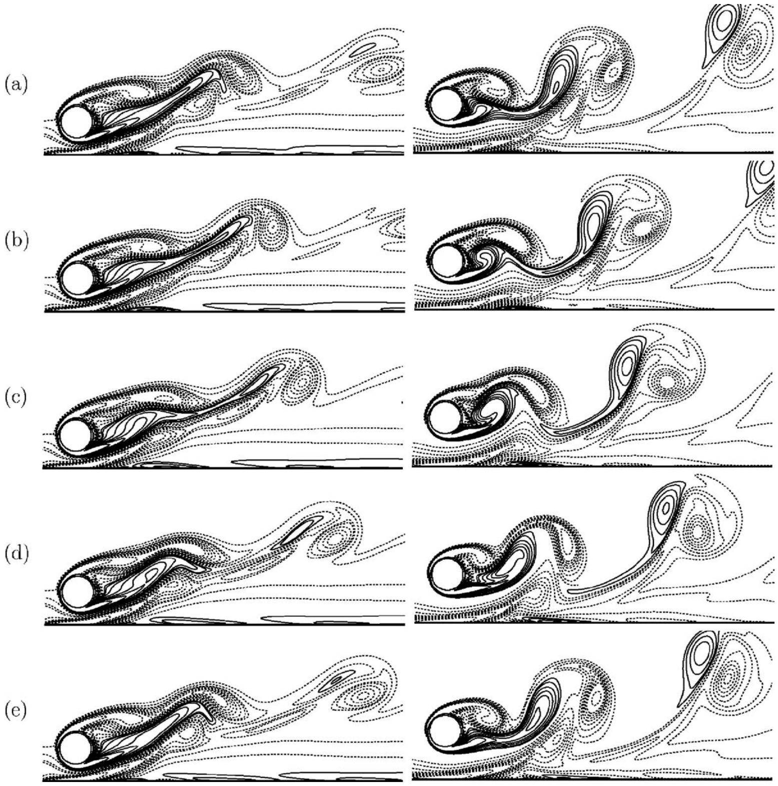

FIG. 9. Vorticity contours around a rotating circular cylinder near a flat wall during one cycle of vortex shedding. Re=200, γ=0.5, and h=0.5 (left) and 1.0 (right). (a) t=0, (b) t=T/5, (c) t=2T/5, (d) t=3T/5, and (e) t=4T/5.

negative vortex generated at the wall are gathered as a group, as shown in Fig. 9(a)(right). At $t=T/5$, the wall-induced (negative) vortex and the positive vortex shed from the cylinder interact with each other, as shown in Fig. 9(b)(right), and two negative vortices in the group merge together to form a larger vortex at $t=2T/5$, as shown in Fig. 9(c)(right). In the meantime, the positive vortex generated from the bottom of the cylinder grows considerably in size and induces a new negative vortex from the wall, as shown in Figs. 9(c)–9(e)(right). In contrast to the case of $h=0.5$, this positive vortex is stronger when $h=1.0$. As the process evolves, a vortex pair of two vortices with unequal strength is formed and shed into the wake, and concurrently, another positive vortex starts to roll up on the lower side of the cylinder at $t=4T/5$, as shown in Fig. 9(e)(right). The period $T\approx 10.0$. An interesting feature to note is that the trajectories of shed vortices cross each other and the final vertical position is opposite to that in the case of a rotating cylinder in an unbounded domain.[3] The negative vortices, shed from the upper side of the cylinder, occupy the lower position in the street while the positive vortices occupy the upper side of the street. This is due to the effect of dominating negative vorticity generated at the wall.

We next show vorticity contours for $\gamma=-1.0$ with h

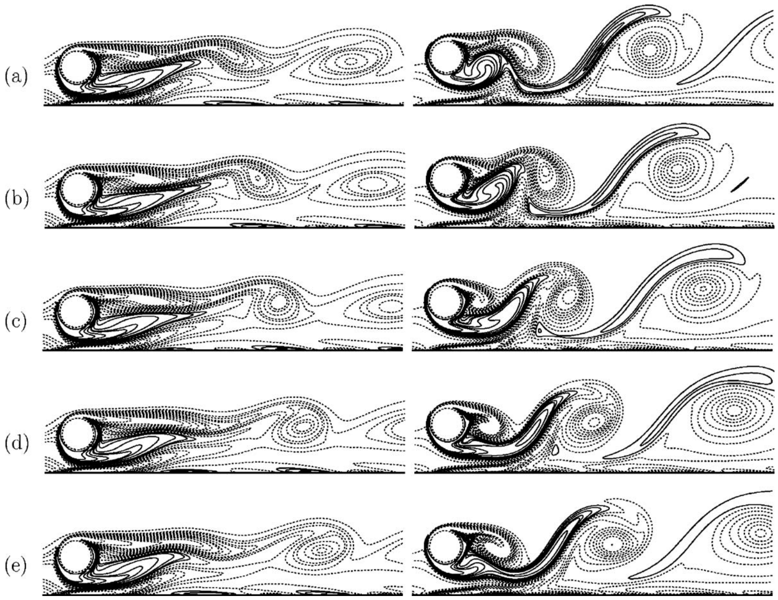

FIG. 10. Similar to Fig. 9, with γ=−1.0, and h=0.7 (left) and 1.0 (right). (a) t=0, (b) t=T/5, (c) t=2T/5, (d) t=3T/5, and (e) t=4T/5.

$=0.7$ and 1.0 in the left and right column of Fig. 10, respectively. For $\gamma=-1.0$ and $h=0.7$, the process of vortex forming and shedding differs significantly from that for $\gamma=0.5$ of Fig. 9. At $t=0$, a positive vortex is generated at the lower side of the cylinder and a much weaker negative vortex at the upper side, while a well-defined negative vortex is being shed into the wake. The wake is clearly dominated by the vorticity shed from upper side of the cylinder, because the interaction between the growing vortex on the upper side of the cylinder and shear layer on the plane wall restricts the strength of positive vortex on the lower side of the cylinder. In addition, the clockwise rotation of the cylinder severely reduces the velocity in the gap so that the positive vortex cannot be efficiently swept downstream by the free stream. One notable feature of this flow configuration is that two interacting vortices with opposite sign attached to the cylinder are considerably distended in streamwise direction, resulting in a large formation region of vortices behind the cylinder. At about $t=4T/5$, a negative vortex on the upper side of the cylinder is transported downstream. In this case, only the negative vortices are shed from the cylinder. Therefore, a single vortex street appears in the wake, also shown in Fig. 7(b).

The process of vortex shedding for $\gamma=-1.0$ and $h=1.0$, as shown in the right column of Fig. 10, is somewhat similar to that for $\gamma=0.5$ and the same h of right column, Fig. 9. At $t=0$, a positive vortex is in the process of development on the lower side of the cylinder, while a negative vortex is about to detach from the cylinder, as shown in the right of Fig. 10(a). At a later time $t=T/5$, shown in the right of Fig. 10(b), the positive vortex draws a thin shear layer of opposite sign from the upper side of the wake across the wake centerline which eventually cuts the supply of vorticity to the positive vortex, as shown in the right of Figs. 10(b)–10(d). Formation of the positive vortex is completed at $t=4T/5$, as shown in the right of Fig. 10(e), after which the vortex is swept downstream. The vortices shed from the upper side of the cylinder are larger than those from the lower side. The positive and negative vortices are shed alternatively, with positive ones elongated in shape and the negative ones rounder. The interaction between vortices of different intensity leads to a vortex street with irregular lateral and longitudinal vortex spacing in the wake. The irregularity of the wake will be further discussed in Sec. III D.

C. Velocity field between the gap and surface pressure distribution

A characteristic feature of the flow around an isolated rotating circular cylinder is the asymmetry of the velocity profiles, leading to asymmetry in the boundary layer separation. The fluid in a region near the cylinder is dragged by the cylinder due to viscous force, and the larger the γ, the greater the region affected by the viscous force.[4] When a plane wall is present in the flow, the symmetry of the flow is completely altered, and the flow fields now depend on both γ and h. The detailed velocity profiles between the cylinder and the wall for $\gamma=1.0$ and -1.0 at different gaps are given in the left and right column of Fig. 11, respectively, for various values of h. When $\gamma=1.0$, the rotation of the cylinder enhances the jet through the gap. The jet is attached to the cylinder at $h=0.2$. When $h=0.4$, the jet is separated from the cylinder with an angle of about 30°. The jet moves into wake, resulting in the deflection of the flow upwards. The separation angle of the jet depends on h. As h increases, the angle seem to reach to a maximum at $h\approx0.5$. The angle would decrease as h further increases beyond 0.5. This behavior of the jet behind the cylinder affects not only the position of vortex shedding into the wake but also the forces on the cylinder. The details of this phenomenon will be further discussed in Sec. III D.

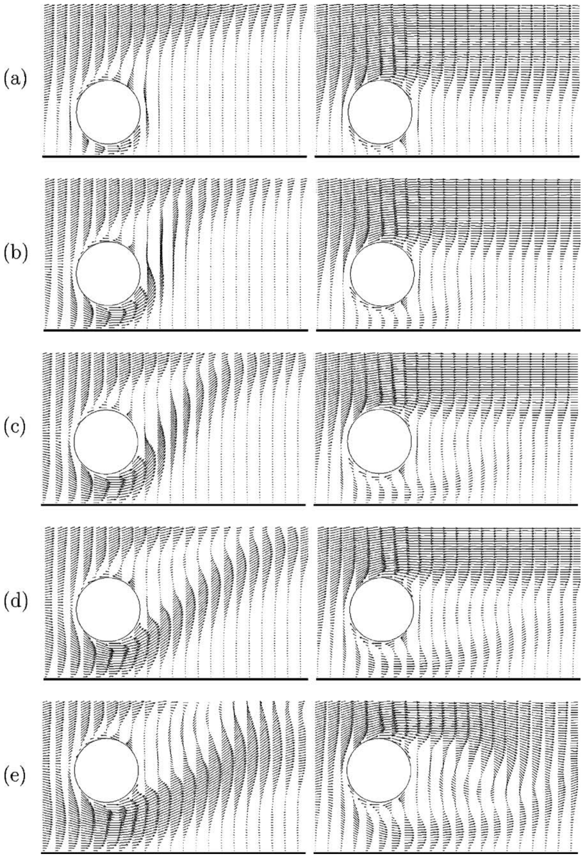

FIG. 11. The gap height (h) dependence of the velocity field around a rotating cylinder near a flat wall with $\gamma=1$ (left) and -1 (right). (a) $h=0.2$, (b) $h=0.4$, (c) $h=0.5$, (d) $h=0.6$, and (e) $h=0.8$.

When $\gamma=-1.0$, as shown in the right column of Fig. 11, the rotation of the cylinder reduces the flow through the gap. The flow in front of the cylinder is deflected upward. Furthermore, the recirculation zone on the plane wall for $\gamma<0$ is smaller than that for $\gamma>0$. Our results suggest that, although the plane wall can affect the magnitude of the velocity field in the gap, the pattern of the velocity field is determined by the direction of the cylinder rotation.

Figure 12 shows the dependence on h and γ of the averaged pressure coefficient $\bar{C}_p$ on the cylinder surface. In the case of flow around a stationary circular cylinder ($\gamma=0$), the boundary layers separated after experiencing a region of adverse pressure gradient. However, when $\gamma<0$, the adverse pressure gradient region increases on one side of the cylinder while it disappears on the other, as $|\gamma|$ increases. We note that the change of the adverse pressure gradient region is not

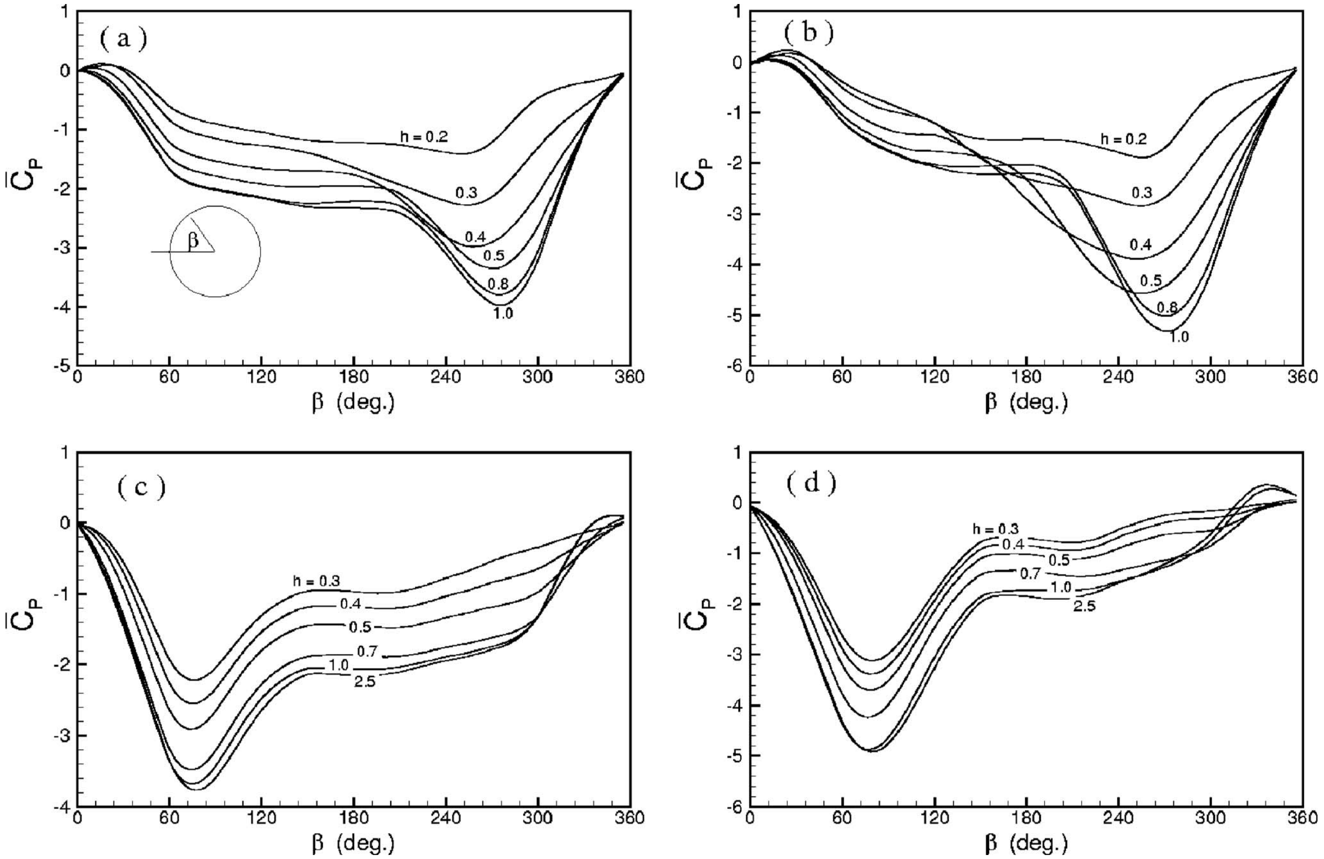

FIG. 12. The dependence of the mean surface pressure distribution $\bar{C}_p(\beta)$ on the rotation rate γ. (a) $\gamma=0.5$, (b) $\gamma=1.0$, (c) $\gamma=-0.5$, and (d) $\gamma=-1.0$.

related to the delay or early separation of the boundary layer as commonly found for the flow past a stationary cylinder. In the case of $\gamma>0$, at the bottom of the cylinder, the rotation of the cylinder accelerates the flow through the gap thereby imparting momentum to the boundary layer at the wall and delaying separation even though it is subject to a large adverse pressure gradient region. At the top of the cylinder, the rotation of the cylinder decelerates flow next to the boundary layer and promotes early separation even though an adverse pressure gradient is absent. Therefore the change of the adverse pressure gradient region is determined by the competition between the momentum generation by the rotating cylinder and the momentum dissipation by the adverse pressure gradient in the boundary layer.

For obvious reasons, the pressure is always lower where the flow is accelerated by the rotation, and higher where the flow is decelerated. The magnitude of suction on both sides of the cylinder varies monotonically with h and γ. As indicated by the data in Table II, the minimum pressure decreases monotonically as either h or γ increases. When $\gamma<0$, the averaged pressure distribution is similar to that for $\gamma>0$, except that the lower pressure is on the top of the cylinder. Also, with a same value of h, the maximum suction pressure for $\gamma<0$ is lower than that for $\gamma>0$. In all cases, the results clearly show that the lift force depends on h and γ monotonically.

TABLE II. Dependence of the minimum averaged surface pressure on γ and h, corresponding to Figs. 12(a) and 12(b).

	h				
γ	0.2	0.3	0.4	0.5	1.0
0.5	−1.4	−2.3	−3.1	−3.4	−3.9
1.0	−1.8	−2.9	−3.8	−4.6	−5.3

D. The lift and drag coefficients

We next investigate the dependence on γ and h of the lift and drag coefficients, C_L and C_D. We are seeking the signatures of various flow patterns in C_L and C_D. The time histories of C_L and C_D and their trajectory are shown in Figs. 13–16. For $\gamma=0.5$, as shown in Fig. 13, both C_L and C_D are almost constants at $h=0.4$, indicating a steady wake corresponding to Fig. 5(a). When $h=0.5$, the lift and drag coefficients exhibit an irregular characteristic that can be seen from their trajectory, as shown in Fig. 13(b), indicating an unstable transition that occurs in the near wake. As h increases to 0.8, C_L and C_D exhibit a regular periodic behavior, as shown in Fig. 13(c), and they have the same frequency. This regular periodic behavior of C_L and C_D remains at $h=1.0$. This regular periodic behavior of C_L and C_D is an indication of the periodic alternating vortex shedding corresponding to Fig. 5(d). In general, after the flow becomes unsteady, we observe that the amplitudes of the fluctuating C_L and C_D grow as h increases, and so do the second harmonic amplitudes in the fluctuating C_L and C_D. This can be

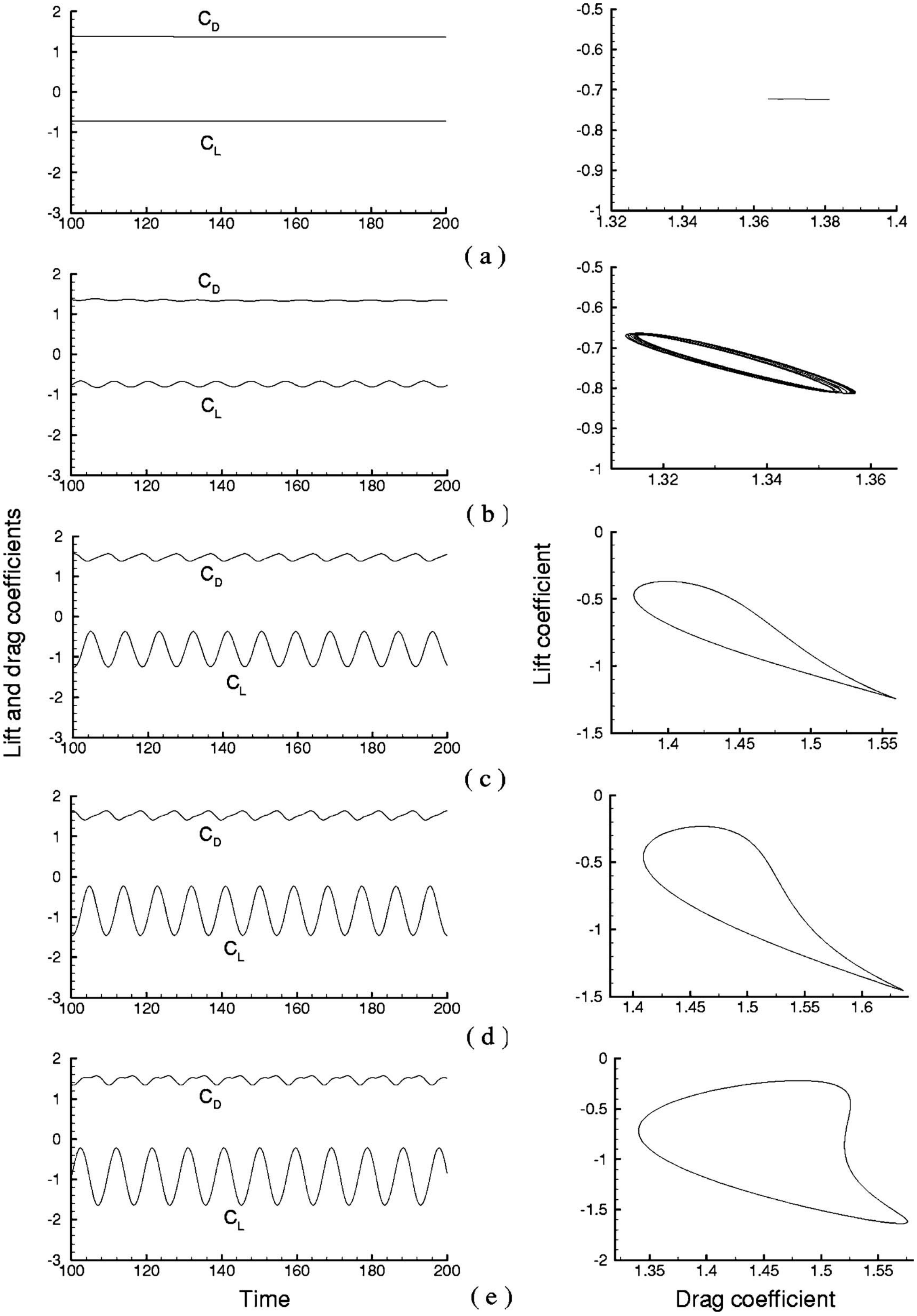

FIG. 13. Dependence on h of the time history of C_D and C_L and the trajectory of the force with $\gamma=0.5$. (a) $h=0.4$, (b) $h=0.5$, (c) $h=0.8$, (d) $h=1.0$, and (e) $h=2.5$.

clearly seen by comparing Figs. 13(c) and 13(d): Obviously the amplitudes of the fluctuating C_D and C_L at $h=1.0$ are larger than that at $h=0.5$, and so does the second harmonic amplitude in the fluctuating C_D. Although the same is true for the second harmonic amplitude in the fluctuating C_L, is it not visible in the figures because the difference between two unequal peaks in C_L are too small to be seen. The second harmonics is due to the two unequal-strength negative vortices generated in the near wake in each shedding cycle, which is more clearly shown in the fluctuating C_D. The two unequal

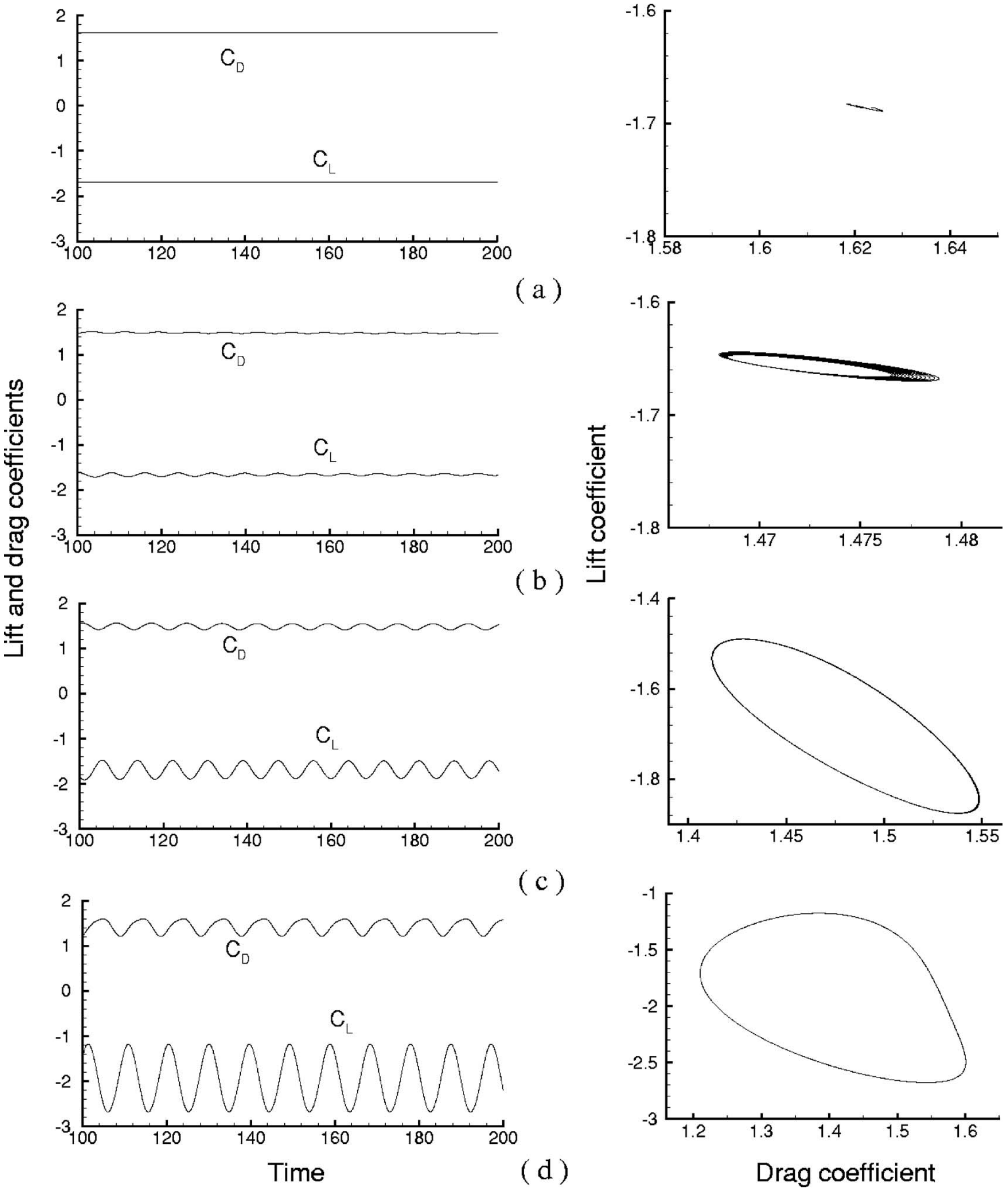

FIG. 14. Similar to Fig. 13, with $\gamma=1.0$ at different h. (a) $h=0.6$, (b) $h=0.7$, (c) $h=0.8$, and (d) $h=2.5$.

adjacent peaks of the fluctuating C_L indicate that the two opposite-signed vortices shed per cycle have different strengths.

The case of $h=2.5$ is similar to that of $h=1.0$. The drag coefficient is similar to that of the flow past a rotating circular cylinder in a unbounded domain.[3]

The lift and drag coefficients as functions of time for $\gamma=1.0$ are shown in Fig. 14. At $h=0.6$, both the lift and drag coefficients are close to be constants, as shown Fig. 14(a). In comparing with the case of $\gamma=0.5$, we can conclude that the larger γ leads the larger h at which vortex shedding is suppressed. When $h=0.7$, the aperiodic fluctuations in C_D and C_L suggest that the unstable transition occurs in the near wake. This instability arises due to the interaction between the vortices generated at the cylinder surface and the vorticity generated at the flat wall. As h increases, the magnitudes of the fluctuations in the lift and drag coefficients clearly increases. This is similar to the case of $\gamma=0.5$. When $h>0.8$, as shown in Fig. 14, the lift and drag coefficients fluctuate periodically with an approximate constant amplitude. The mean value of the lift coefficient, $\bar{C}_L$ decreases monotonically as h increases, except in a narrow range of $0.6<h<0.8$.

The time histories of the lift and drag coefficients for $\gamma=-0.5$ and -1.0 are presented in Figs. 15 and 16, respectively. When $\gamma=-0.5$, the lift and drag coefficients are constants at $h=0.4$, as shown in Fig. 15(a), indicating a stable wake flow corresponding to Fig. 7(a). The values of the lift and drag coefficients are close to each other. When $h=0.5$, the lift and drag coefficient are aperiodic, as shown in Fig. 15(b), as a consequence of an unstable single vortex shed-

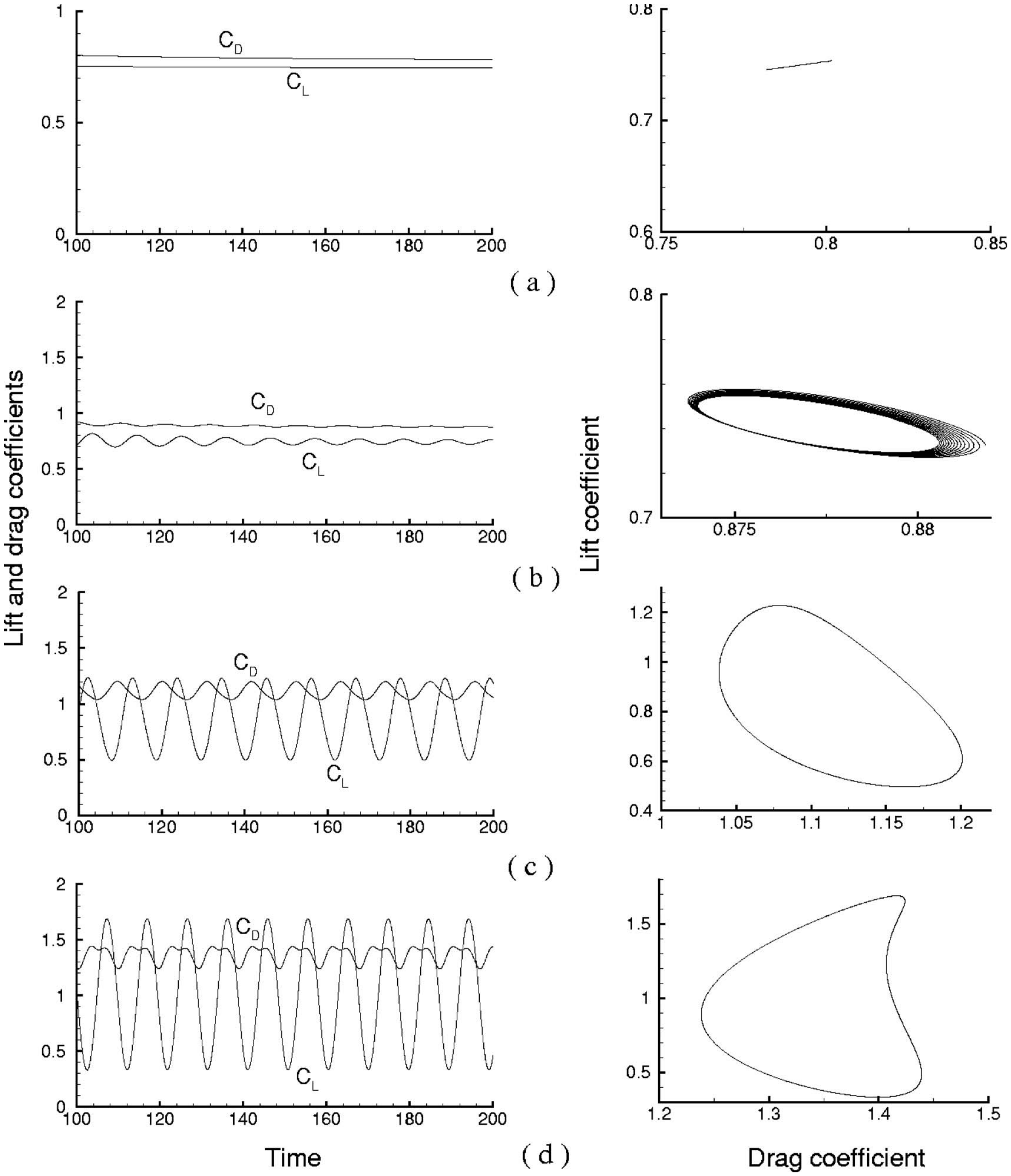

FIG. 15. Similar to Fig. 13, with $\gamma = -0.5$ at different h. (a) $h=0.4$, (b) $h=0.5$, (c) $h=0.7$, and (d) $h=2.5$.

ding shown in Fig. 7(b). As h increases up to 2.5, the fluctuation magnitudes in C_L and C_D increase monotonically, as indicated in Figs. 15(a)–15(d). However, only when $h > 1.0$, the second-harmonics in both C_L and C_D appears, as shown in Fig. 15(d).

Figure 16 shows C_L and C_D as functions of time for $\gamma = -1.0$ with varying h. The overall time-dependent characteristics of C_L and C_D for $\gamma = -1.0$ are similar to that of $\gamma = -0.5$, but there are some quantitative differences. First, the fluctuation magnitudes of C_L and C_D are larger with $\gamma = -1.0$, although the mean values of both C_L and C_D increase monotonically as functions of h in both cases, as shown in Figs. 17(a) and 17(b). This is related to the details of the vortex shedding location, wake width and separation position, as shown in Fig. 10. And second, for $\gamma = -0.5$, $\bar{C}_D > \bar{C}_L$. For $\gamma = -1.0$, when $h \leqslant 0.6$, $C_D > C_L$, and when $h \geqslant 0.7$, however, $C_D < C_L$ almost all the time.

We now study the dependence on h of the time-averaged mean and root-mean-square (RMS) of the lift and drag coefficients. Our results are presented in Fig. 17. The mean value of the drag coefficient, $\bar{C}_D$, is a monotonically increasing function of h when $\gamma \leqslant 0$, as shown in Fig. 17(a). For $\gamma > 0$, the $\bar{C}_D$ is no longer monotonic in h; it develops two local maximum and a local minimum when $0 < h < 2.5$. The nonmonotonicity of $\bar{C}_D(h)$ when $\gamma > 0$ is due to the reason that the angle of the jet through the gap strongly depends on h nonlinearly when h is small. We also observe that for h

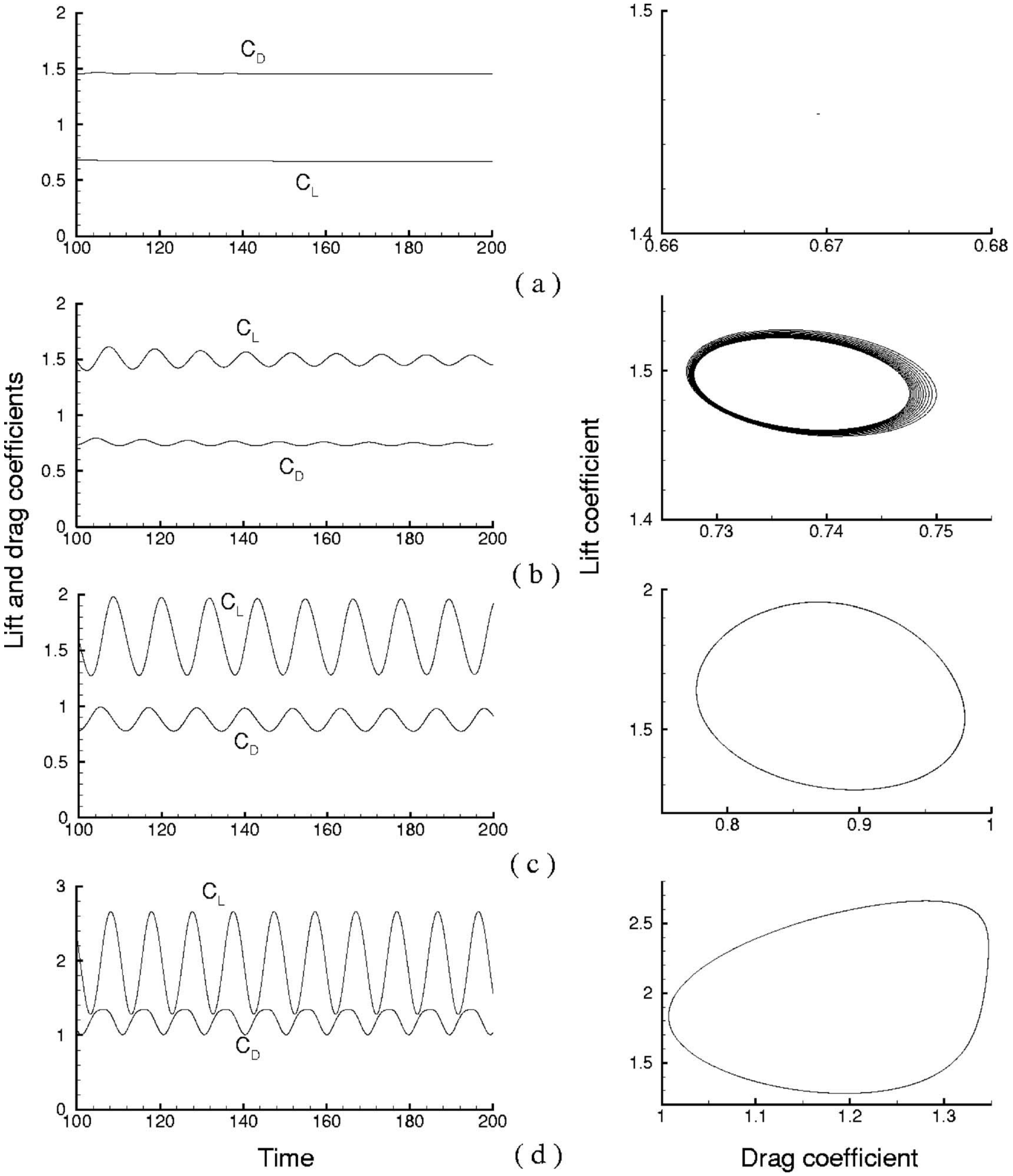

FIG. 16. Similar to Fig. 13, with $\gamma=-1.0$ at different h. (a) $h=0.6$, (b) $h=0.7$, (c) $h=0.8$, and (d) $h=2.5$.

>2.5, the value of $\bar{C}_D$ approaches a constant depending on γ, manifesting the diminishing effect of wall as large h. In addition, $\bar{C}_D$ is also a monotonically increasing function of γ when $-1.0\leqslant\gamma\leqslant 1.0$ and $h<2.0$, as shown in Fig. 17(a).

Figure 17(b) shows the mean value of the lift coefficient $\bar{C}_L$ as a function of γ and h. First of all, $\bar{C}_L$ is a monotonically decreasing function of γ. It is also a monotonically decreasing function of h when $\gamma<0$. When $\gamma\geqslant 0$, $\bar{C}_L$ is not a monotonic function of h although it is mostly decreasing. It should also be noted that h-dependence of $\bar{C}_L$ is much stronger when $\gamma>0$. Similar to $\bar{C}_D$, beyond a certain value of h, $\bar{C}_L$ approaches a constant depending on γ.

Figure 17(c) shows the RMS values of the lift and drag coefficients, $\tilde{C}_L$ and $\tilde{C}_D$, as functions of h and γ. With a given γ, both $\tilde{C}_L$ and $\tilde{C}_D$ approach zero when h is smaller than a certain critical value, which depends on γ, indicating that the flow is in steady state in such a configuration. At a certain critical value of h, which is γ-dependent, both $\tilde{C}_D$ and especially $\tilde{C}_L$ increase drastically, indicating a steady-unsteady state transition. The RMS value of the lift undergoes a steep increase when $0.5<h<1.5$. Beyond $h=1.5$, both $\tilde{C}_L$ and $\tilde{C}_D$ approach to γ-dependent constants. Figure 17(d) shows the ratio of the mean drag and the lift coefficients, $\bar{C}_L/\bar{C}_D$. The ratio $\bar{C}_L/\bar{C}_D$ is a monotonically decreasing function of γ, and of h when $\gamma<0$. When $\gamma\geqslant 0$, $\bar{C}_L/\bar{C}_D$ is a decreasing function of h except when $0.8\leqslant h\leqslant 1.5$, in which $\bar{C}_L/\bar{C}_D$ increases slightly.

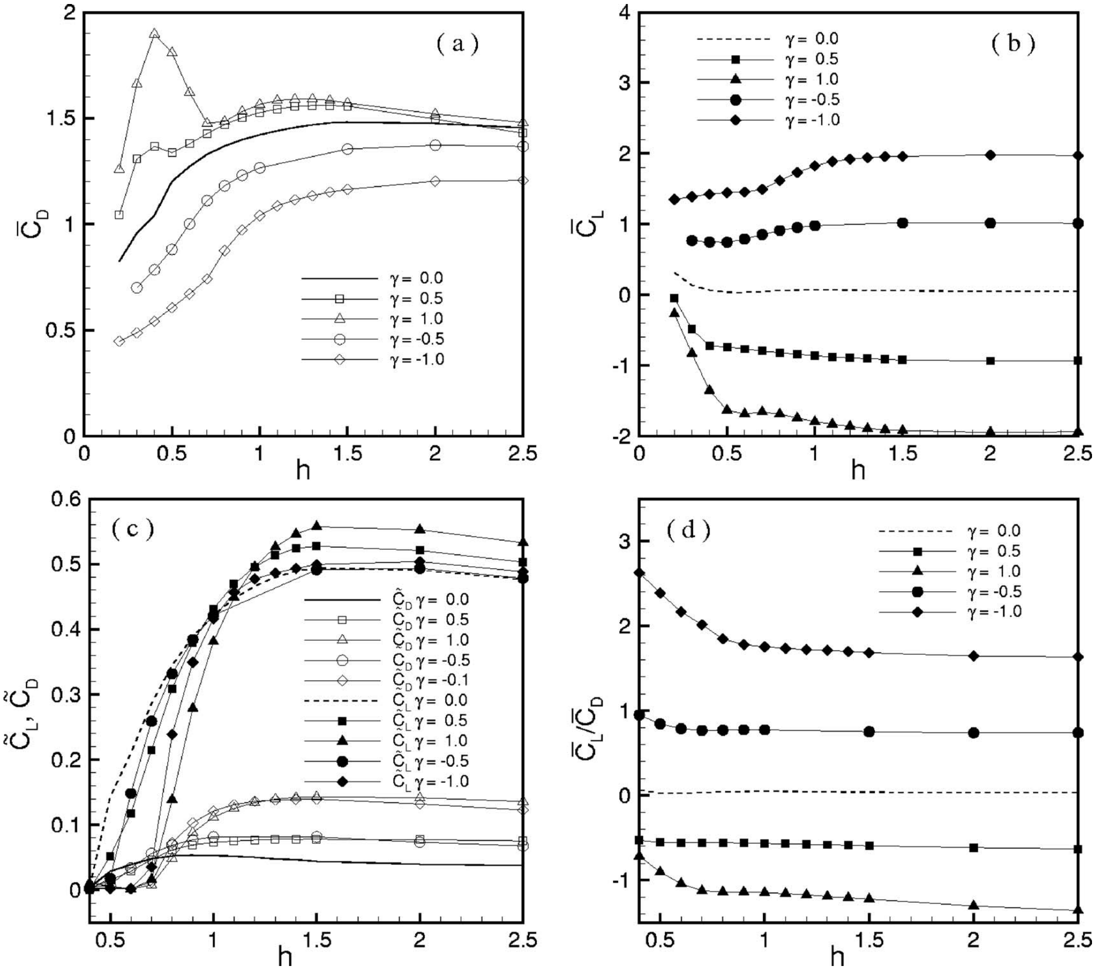

FIG. 17. Dependence of variations of the lift and drag coefficients on the gaps h. (a) Mean value of the drag coefficient $\bar{C}_D$, (b) mean value of the lift coefficient $\bar{C}_L$, (c) root-mean-square values of the lift and drag coefficients, $\tilde{C}_L$ and $\tilde{C}_D$, and (d) the ratio of mean lift and mean drag coefficients, $\bar{C}_L/\bar{C}_D$.

IV. CONCLUSIONS

The flow past a rotating circular cylinder near a plane wall at Re=200 is investigated numerically by using the lattice Boltzmann method. The typical wake patterns for the rotating cylinder near a wall are succinctly summarized in Fig. 18. The flow feature characterized by the vortex structure can be classified into three categories on the parameter space of h and γ: steady state, aperiodic, and periodic vortex shedding.

Our results indicate the existence of two critical gap values, h_{down} and h_{up}, both of which depend on γ. When $h < h_{\text{down}}$, the flow is steady and the gap flow is either completely suppressed or extremely weak, and separation of the boundary layer occurs both upstream and downstream of the cylinder. There is no vortex shedding in the wake. The wake flow is a stable. The larger the value of γ, the higher the h at which vortex shedding is suppressed. When $h_{\text{down}} < h < h_{\text{up}}$, the vortex pattern appears be aperiodic, as indicated by the incommensurate frequencies of the lift and drag forces. When $h > h_{\text{up}}$, there is no boundary layer separation on the plane wall, either upstream or downstream of the cylinder. A regular vortex street appears in the wake. The value of h_{up} weakly depends on γ.

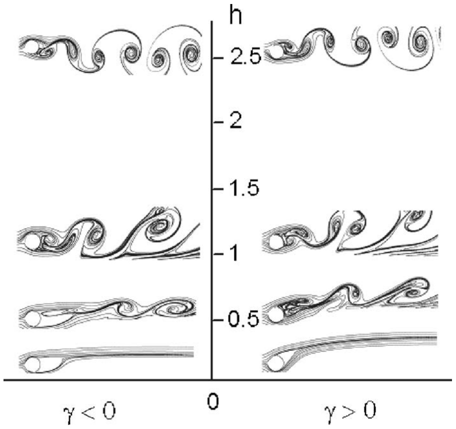

FIG. 18. The near-wake vortex structure in γ-h parameter space.

We observe that the lift and drag forces exerted on the cylinder depend strongly on both the gap height h and the rotation rate γ. When the gap is small, the wall exerts a stronger influence on the lift and drag forces for a rotating cylinder than a stationary one. The mean drag coefficient $\bar{C}_D$ is a monotonically increasing function of h when $\gamma \leqslant 0$.

When $\gamma > 0$, $\bar{C}_D$ is no longer a monotonic function of h. The mean drag coefficient $\bar{C}_D$ varies significantly in the range $h_{\text{down}} < h < h_{\text{up}}$, and so do the RMS values of the lift and drag coefficients, $\tilde{C}_D$ and $\tilde{C}_L$.

ACKNOWLEDGMENTS

We would like to thank an anonymous referee, whose comments help improve this paper significantly. L.-S.L. is supported by the U.S. DOD under the AFOSR-MURI project "Hypersonic transition and turbulence with nonequilibrium thermochemistry" (Dr. J. Schmisseur, Program Manager) and by NASA Langley Research Center under a C&I grant through the NIA Cooperative Agreement Grant No. NCC-1-02043.

[1] L. Prandtl, "The Magnus effect and windpowered ships," Naturwiss. **13**, 93 (1925).
[2] H. M. Badr and S. C. R. Dennis, "Time-dependent viscous flow past an impulsively started rotating and translating circular cylinder," J. Fluid Mech. **158**, 447 (1985).
[3] Y. M. Chen, Y. R. Ou, and A. J. Pearlstein, "Development of the wake behind a circular cylinder impulsively started into rotatory and rectilinear motion," J. Fluid Mech. **253**, 449 (1993).
[4] Y. T. Chew, M. Cheng, and S. C. Luo, "A numerical study of vortex shedding from a rotating circular cylinder by a hybrid vortex method," J. Fluid Mech. **299**, 35 (1995).
[5] F. Diaz, J. Gavalda, J. G. Kawall, J. F. Keffer, and F. Giralt, "Vortex shedding from a spinning cylinder," Phys. Fluids **26**, 3454 (1983).
[6] M. C. Ece, J. D. A. Walker, and T. L. Doligalski, "The boundary layer on an impulsively started rotating and translating cylinder," Phys. Fluids **27**, 1077 (1984).
[7] S. Mittal and B. Kumar, "Flow past a rotating cylinder," J. Fluid Mech. **476**, 303 (2003).
[8] W. B. Glauer, "The flow past a rapidly rotating circular cylinder," Proc. R. Soc. London, Ser. A **242**, 108 (1957).
[9] P. K. Stansby and R. C. T. Rainey, "A CFD stydey of the dynamic response of a rotating cylinder in a current," J. Fluids Struct. **15**, 513 (2001).
[10] P. W. Bearman and M. M. Zdravkovich, "Flow around a circular cylinder near a plane boundary," J. Fluid Mech. **89**, 33 (1978).
[11] G. Buresti and A. Lanciotti, "Vortex shedding from smooth and roughened cylinders in cross-flow near a plane surface," Aeronaut. Q. **30**, 305 (1979).
[12] M. Cheng, H. E. Tsuei, and K. L. Chow, "Experimental study on flow interference phenomena of cylinder/cylinder and cylinder/plane arrangements," in *Flow-Induced Vibration*, edited by M. K. Au-Yang (ASME, New York, 1994), pp. 173–184.
[13] A. J. Grass, P. W. J. Raven, R. J. Stuart, and J. A. Bray, "The influence of boundary layer velocity gradients and bed proximity on vortex shedding from free spanning pipelines," J. Energy Resour. Technol. **106**, 70 (1984).
[14] C. Lei, L. Cheng, and K. Kavanagh, "Re-examination of the effect of a plane boundary on force and vortex shedding of a circular cylinder," J. Wind. Eng. Ind. Aerodyn. **80**, 263 (1999).
[15] S. J. Price, D. Sumner, J. G. Smith, K. Leong, and M. P. Paidoussis, "Flow visualization around a circular cylinder near to a plane wall," J. Fluids Struct. **16**, 175 (2002).
[16] S. Taneda, "Experimental investigation of vortex streets," J. Phys. Soc. Jpn. **20**, 1714 (1965).
[17] S. Taniguchi and K. Miyakoshi, "Fluctuating fluid forces acting on a circular cylinder and interference with a plane wall," Exp. Fluids **9**, 197 (1990).
[18] M. M. Zdravkovich, "Forces on a circular cylinder near a plane wall," Appl. Ocean. Res. **7**, 197 (1985).
[19] A. Dipankar and T. K. Sengupta, "Flow past a circular cylinder in the vicinity of a plane wall," J. Fluids Struct. **20**, 403 (2005).
[20] L. Zhou, M. Cheng, and K. C. Hung, "Suppression of fluid force on a square cylinder by flow control," J. Fluids Struct. **21**, 151 (2005).
[21] C. H. K. Williamson, "Vortex dynamics in the cylinder wake," Annu. Rev. Fluid Mech. **28**, 477 (1996).
[22] D. d'Humières, "Generalized lattice-Boltzmann equations," in *Rarefied Gas Dynamics, Theory and Simulations*, Prog. Astronaut. Aeronaut., edited by B. D. Shizgal and D. P. Weave (AIAA, Washington, D.C., 1992), Vol. 159, pp. 450–458.
[23] D. d'Humières, I. Ginzburg, M. Krafczyk, P. Lallemand, and L.-S. Luo, "Multiple-relaxation-time lattice Boltzmann models in three-dimensions," Philos. Trans. R. Soc. London **360**, 437 (2002).
[24] P. Lallemand and L.-S. Luo, "Theory of the lattice Boltzmann method, dispersion, dissipation, isotropy, Galilean invariance, and stability," Phys. Rev. E **61**, 6546 (2000).
[25] P. Lallemand and L.-S. Luo, "Lattice Boltzmann method for moving boundaries," J. Comput. Phys. **184**, 406 (2003).
[26] S. Chen and G. D. Doolen, "Lattice Boltzmann method for fluid flows," Annu. Rev. Fluid Mech. **30**, 329 (1998).
[27] D. Yu, R. Mei, L.-S. Luo, and W. Shyy, "Viscous flow computations with the method of lattice Boltzmann equation," Prog. Aerosp. Sci. **39**, 329 (2003).
[28] B. van Leer, "Computational fluid dynamics: Science or toolbox?" AIAA Pap. 2001–2520 (2001).
[29] I. Ginzbourg and P. M. Adler, "Boundary flow condition analysis for the three-dimensional lattice Boltzmann model," J. Phys. II **4**, 191 (1994).
[30] I. Ginzbourg and D. d'Humières, "Local second-order boundary methods for lattice Boltzmann models," J. Stat. Phys. **84**, 927 (1996).
[31] I. Ginzburg and D. d'Humières, "Multireflection boundary conditions for lattice Boltzmann models," Phys. Rev. E **68**, 066614 (2003).
[32] C. Pan, L.-S. Luo, and C. T. Miller, "An evaluation of lattice Boltzmann schemes for porous medium flow simulation," Comput. Fluids **35**, 898 (2006).
[33] X. He and L.-S. Luo, "Lattice Boltzmann model for the incompressible Navier-Stokes equation," J. Stat. Phys. **88**, 927 (1997).
[34] P. L. Bhatnagar, E. P. Gross, and M. Krook, "A model for collision processes in gases. I. Small amplitude processes in charged and neutral one-component systems," Phys. Rev. **94**, 511 (1954).
[35] Y. H. Qian, D. d'Humières, and P. Lallemand, "Lattice BGK models for Navier-Stokes equation," Europhys. Lett. **17**, 479 (1992).
[36] H. Chen, S. Chen, and H. W. Matthaeus, "Recovery of the Navier-Stokes equations using a lattice-gas Boltzmann method," Phys. Rev. A **45**, R5339 (1992).
[37] L.-S. Luo, "Theory of the lattice Boltzmann method: Lattice Boltzmann models for nonideal gases," Phys. Rev. E **62**, 4982 (2000).
[38] M. Cheng, S. H. N. Tan, and K. C. Hung, "Linear shear flow over a square cylinder at lower Reynolds number," Phys. Fluids **17**, 078103 (2005).
[39] M. A. Gallivan, D. R. Noble, J. G. Georgiadis, and R. O. Buckius, "An evaluation of the bounce-back boundary condition for lattice Boltzmann simulations," Int. J. Numer. Methods Fluids **25**, 249 (1997).